

Article

Aircraft Measurements of Tropospheric CO₂ in the North China Plain in Autumn and Winter of 2018–2019

Hui Zhang^{1,2,3}, Qiang Yang^{1,2,4}, Hongjie Yuan^{1,2,4}, Dongliang Ma³, Zhilei Liu³, Jianguang Jia³, Guan Wang³, Nana Zhang⁵, Hailiang Su³, Youyu Shi³, Yongjing Ma⁶, Lindong Dai⁷, Baojiang Li⁸ and Xiao Huang^{9,*}

¹ China Meteorological Administration Xiong'an Atmospheric Boundary Layer Key Laboratory, Xiong'an New Area 071800, China; zhanghui@cfdqx.cn (H.Z.); yangqiang@cfdqx.cn (Q.Y.); yuanhongjie@cfdqx.cn (H.Y.)

² Key Laboratory of Meteorology and Ecological Environment of Hebei Province, Shijiazhuang 050021, China

³ Tangshan Meteorological Bureau of Hebei Province, Tangshan 063000, China; madongliang@cfdqx.cn (D.M.); liuzhilei@cfdqx.cn (Z.L.); jiajianguang@cfdqx.cn (J.J.); wangguan@cfdqx.cn (G.W.); suhailiang@cfdqx.cn (H.S.); shiyouyu@cfdqx.cn (Y.S.)

⁴ Hebei Provincial Weather Modification Center, Shijiazhuang 050020, China

⁵ Laoting Meteorological Bureau of Hebei Province, Tangshan 063000, China; zhangnana@cfdqx.cn

⁶ State Key Laboratory of Atmospheric Boundary Layer Physics and Atmospheric Chemistry, Institute of Atmospheric Physics, Chinese Academy of Sciences, Beijing 100029, China; mayongjing@mail.iap.ac.cn

⁷ Institute of Urban Meteorology, China Meteorological Administration, Beijing 100080, China; lddai@ium.cn

⁸ Beijing Jiangbo Environmental Technology Co., Ltd., Beijing 101199, China; libaojiang@jbhj.com.cn

⁹ College of Geographical Sciences, Hebei Normal University, Shijiazhuang 050024, China

* Correspondence: huangxiao@stu.hebtu.edu.cn

Abstract: Quantifying the level of CO₂, the main greenhouse gas (GHG), is essential for research on regional and global climate change, especially in the densely populated North China Plain with its severe CO₂ emissions. In this study, 12 airborne flights were managed and conducted during the autumn–winter period of 2018–2019 in downtown Shijiazhuang and its surrounding areas, which are representative of the typical urban conditions in the North China Plain, to explore the spatial and temporal distributions of CO₂. The results showed that the measured columnar averages of CO₂ ranged between 399.9 ± 1.5 and 443.8 ± 31.8 ppm; the average of the 12 flights was 412.1 ppm, slightly higher than the globally averaged 410.5 ± 0.20 ppm and the 2 background concentrations of 411.6 ± 2.1 ppm and 411.4 ± 0.2 ppm in low-latitude Mauna Loa and middle-latitude Waliguan in 2019, indicating the potential influences of anthropogenic activities. The typical stratification of the planetary boundary layer (PBLH), residual layer (RL), and elevated inversion layer (IL) was crucial in constraining the high CO₂ concentrations. This illustrated that the warming effect of CO₂ within the PBLH may also have some influences on regulating the thermal structure of the low troposphere. Based on a backward trajectory analysis, it was evidenced that there were three different categories of air masses for autumn and one category for winter. Both trajectories in the PBL, i.e., below 1000 m, from the local and southern areas with tremendous anthropogenic emissions (autumn) and from the western regions (winter) led to comparatively high levels of CO₂, but the mid-tropospheric CO₂ concentrations above 1000 m were commonly homogeneously distributed, with higher levels appearing in winter because the concentration in the free troposphere followed the global seasonal pattern, with a summer minimum and winter maximum as a result of the seasonality of the net CO₂ exchange and the balance between photosynthesis and respiration. These results provide an in-depth understanding of the vertical concentrations of tropospheric CO₂ in the North China Plain, which will offer scientific references for the evaluation of carbon accounting and carbon emissions.

Keywords: aircraft measurement; tropospheric CO₂; North China Plain; backward trajectory



Citation: Zhang, H.; Yang, Q.; Yuan, H.; Ma, D.; Liu, Z.; Jia, J.; Wang, G.; Zhang, N.; Su, H.; Shi, Y.; et al. Aircraft Measurements of Tropospheric CO₂ in the North China Plain in Autumn and Winter of 2018–2019. *Atmosphere* **2023**, *14*, 1835. <https://doi.org/10.3390/atmos14121835>

Academic Editor: Valéry Catoire

Received: 16 October 2023

Revised: 14 December 2023

Accepted: 16 December 2023

Published: 18 December 2023



Copyright: © 2023 by the authors. Licensee MDPI, Basel, Switzerland. This article is an open access article distributed under the terms and conditions of the Creative Commons Attribution (CC BY) license (<https://creativecommons.org/licenses/by/4.0/>).

1. Introduction

Greenhouse gases (GHGs) are well-known worldwide to considerably increase air temperatures by absorbing long-wave radiation and inducing a warming effect on the Earth's climate, thereby attracting widespread concern from both international scientists and governments. Accurate measurements of their concentrations and flux are, therefore, of great urgency in order to evaluate their contributions to the regulation of the global temperature. Among the wide variety of GHGs, carbon dioxide (CO₂) is regarded as the most important due to its effect on the global radiation balance and its contributions to global warming [1–4]; it accounts for about 66% of the total radiative forcing induced by the increasing amounts of GHGs [5]. According to statistics, the global average CO₂ concentration before industrialization (circa 1750) was around 280 ppm [6]. Due to influences from intense human activities and severe anthropogenic emissions, there has always been an upward trend for the global CO₂ concentration, and in 2022, this was 150% of the pre-industrial level, i.e., 420 ppm [7]. These changes are believed to be closely linked to the overuse of fossil fuels [8,9] and changes in land use [10,11].

The measurement of atmospheric CO₂ concentrations and the quantification of emissions based on an inverse modeling approach are powerful means of assessing and verifying CO₂ emissions [12–14]. At present, multiple platforms have been designed and developed to observe both the concentrations and emissions of CO₂. For example, the international FLUXNET uses the eddy covariance technique to measure the cycling of carbon, water, and energy between the biosphere and atmosphere, and global emission datasets of carbon species have been collected [15–17]. In situ measurements with GHG instruments have also been adopted worldwide to determine CO₂ concentrations at the ground level [18–20]. Additionally, satellite remote sensing is an advanced technology for observing global carbon distributions, but it can only be used to detect columnar information because of the limitations of its technological development [21,22]. Vertical observations serve as a great supplementary means of both in situ ground measurement and columnar remote sensing with satellites. Currently, three approaches are commonly used to measure vertical profiles, i.e., gradient towers, tethered balloons, and aircraft [23]. A gradient tower provides excellent accessibility for monitoring the near-surface concentrations of CO₂ in a continuous time series, but it has deficiencies in flexibility and heights beyond 400 m [24–26]. Tethered balloons offer an excellent vertical resolution for sampling, although they are often difficult to control [27,28]. Aircraft observations have advantages in both the design of flight paths and obtaining high-vertical-resolution atmospheric species [29,30], making them the most advanced means of vertical detection for scientists worldwide. For example, aircraft measurements have been widely applied in European cities, such as Rome, London, and Paris, to observe the concentrations of greenhouse gases [31]. The U.S. National Oceanic and Atmospheric Administration (NOAA) launched the Global Greenhouse Gas Reference Network's aircraft program to measure air samples for the later analysis of carbon dioxide (CO₂), carbon monoxide (CO), nitrous oxide (N₂O), methane (CH₄), molecular hydrogen (H₂), and sulfur hexafluoride (SF₆), as well as isotopes of CO₂ and CH₄ and multiple halo- and hydrocarbons. Extensive aircraft profile observations have been organized and managed in North America, in addition to a few flights in the Pacific Ocean, South America, and Outer Mongolia [32]. Above eastern Amazonia, vertical profiles of CO₂ were collected from 2000 to January 2010 to help determine the regional-scale (~10⁵–10⁶ km²) fluxes of carbon-cycle-related greenhouse gases in Brazil [33].

Though it is one of the countries with the greatest amounts of CO₂ emissions in the world, aircraft CO₂ observations in China have rarely been reported. Especially for the North China Plain, a place with a high population density, developed industrial output, and advanced social economies, systematic measurements of CO₂ and concurrent thermodynamic profiles are urgently needed to account for carbon emissions. In this regard, 12 flights were designed and conducted to assess a representative carbon source—the industrial and populated Shijiazhuang City in the North China Plain—during the autumn and winter seasons of 2018 and 2019. The results deepen the understanding of the vertical distribution of CO₂ in

the North China Plain. Not only are valuable CO₂ datasets for climate models provided but scientific references for policymaking to meet the requirements of carbon peaks and carbon neutrality put forward by the Chinese government in 2020 are also offered.

2. Methodology

2.1. Flight Regions—Shijiazhuang City

Shijiazhuang City (118.2° E, 39.5° N) is located in the south of the North China Plain and at the foot of the Taihang Mountains, as shown in Figure 1. As the capital city of Hebei Province, Shijiazhuang on the North China Plain ranks third in China in terms of urban agglomeration, after Beijing and Tianjin, and it is characterized by its high energy consumption, tremendous anthropogenic activity, and large amounts of carbon emissions. All of these characteristics make it a significant anthropogenic carbon source on the North China Plain. For example, according to statistics, the CO₂ emissions in Shijiazhuang are around 90.00 million tons [34]. Considering the functional orientation, economic and social development, resources, and environment of the region of the North China Plain, it is necessary to take Shijiazhuang City as representative of typical industrial and populated areas on the North China Plain to study the spatio-temporal CO₂ distributions.

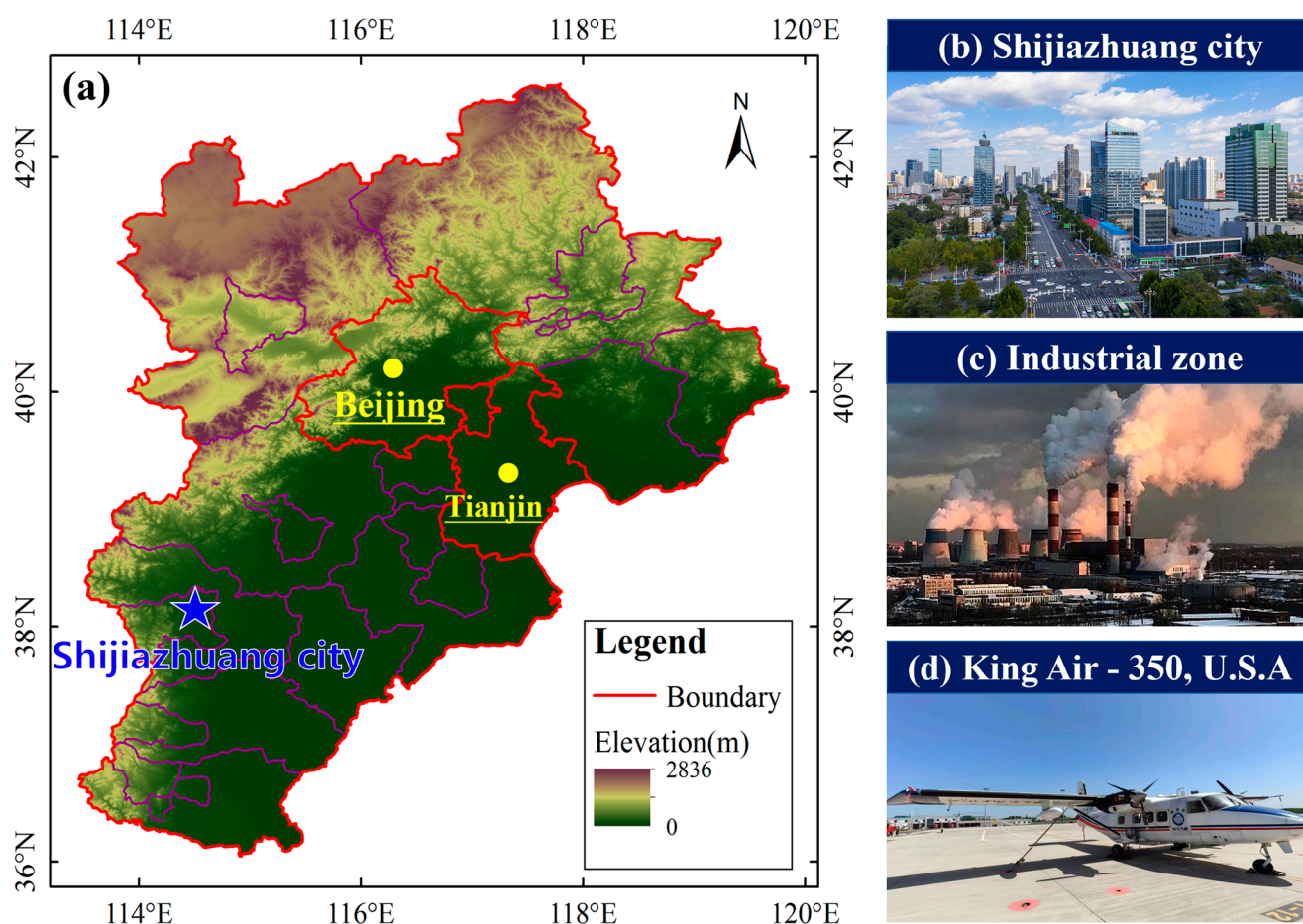


Figure 1. (a) Map of the North China Plain with a blue star representing Shijiazhuang City. (b–d) Photos of downtown Shijiazhuang, the surrounding industrial zone, and the King Air-350 aircraft used in this study.

2.2. Aircraft Measurements

In this study, a King Air-350 aircraft (Augsburg Air Service GmbH, Augsburg, Bavaria, Germany) managed by the Hebei Weather Modification Office was equipped with a cavity ring-down spectroscopy (CRDS) greenhouse gas analyzer (PICARRO company, Santa

Clara, CA, USA) and related equipment for measuring tropospheric CO₂. This type of aircraft had a cruising speed of 220 km/h, a maximum flying height of 7000 m, a maximum flight time of 8 h, and a non-airtight cabin. The accuracy of the CRDS greenhouse gas analyzer for atmospheric CO₂ was 0.1 ppm, and the time resolution was 2.7 s. A Beidou navigation system mounted on the aircraft collected information on the longitude, latitude, altitude, and flight speed during flight. All of the equipment was regularly maintained and calibrated before every measurement flight.

In the autumn and winter seasons of 2018–2019, a total of 12 spiral flights were performed above Shijiazhuang City, as shown in Table 1 and Figure 2, with 8 consecutive flights (Flight 01 on 8 September 2018, Flights 02 and 03 on 9 September 2018, Flights 04 and 05 on 10 September 2018, Flight 06 in 12 September 2018, and Flights 07 and 08 on 14 September 2018) in autumn and 4 flights (Flight 09 on 8 January 2019, Flight 10 on 9 January 2019, Flight 11 on 11 January 2019, and Flight 12 on 12 January 2019) in winter. The durations of Flight 01 to Flight 12 were 11:06–12:46, 08:14–11:10, 12:56–14:49, 05:09–07:49, 11:17–13:12, 12:12–12:44, 03:13–06:10, 10:53–14:13, 11:00–18:06, 03:25–04:58, 02:47–06:24, and 05:48–09:21, with corresponding vertical ranges of 1200–5500 m, 0–5100 m, 600–5000 m, 0–4600 m, 600–2800 m, 0–2800 m, 0–5200 m, 0–5000 m, 0–5400 m, 0–5100 m, 0–5300 m, and 1100–5000 m.

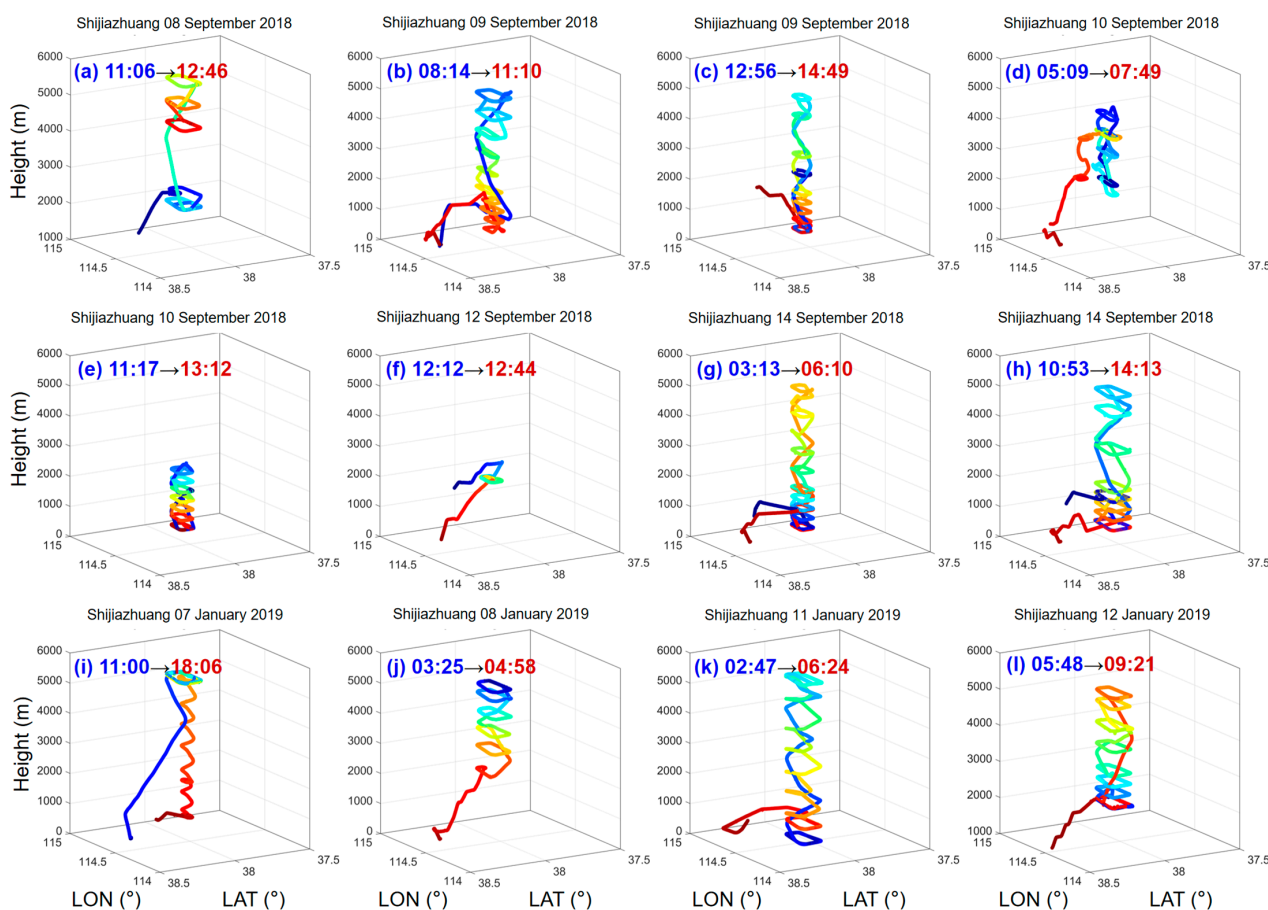


Figure 2. Flight paths for the 12 aircraft measurements during (a) Flight 01 (8 September 2018), (b) Flight 02 (9 September 2018), (c) Flight 03 (9 September 2018), (d) Flight 04 (10 September 2018), (e) Flight 05 (10 September 2018), (f) Flight 06 (12 September 2018), (g) Flight 07 (14 September 2018), (h) Flight 08 (14 September 2018), (i) Flight 09 (7 January 2019), (j) Flight 10 (8 January 2019), (k) Flight 11 (11 January 2019), and (l) Flight 12 (12 January 2019). The color code represents the path from takeoff (blue) to landing (red).

Table 1. The measured profiles of a tropospheric greenhouse gas (CO₂) in Shijiazhuang City in 2018–2019.

| Season | Flight ID | Date | Duration | Lat. Range (°) | Lon. Range (°) | Alt. Range (m) | CO ₂ (ppm) AVE ± STD | CO ₂ (ppm) Range |
|--------|-----------|-------------------|-------------|----------------|----------------|----------------|---------------------------------|-----------------------------|
| Autumn | Flight 01 | 8 September 2018 | 11:06–12:46 | 38.0–38.2 | 114.4–114.8 | 1200–5500 | 399.9 ± 1.5 | 396.9–404.4 |
| | Flight 02 | 9 September 2018 | 08:14–11:10 | 38.0–38.5 | 114.4–114.7 | 0–5100 | 404.4 ± 6.7 | 386.8–449.8 |
| | Flight 03 | 9 September 2018 | 12:56–14:49 | 38.0–38.2 | 114.4–114.7 | 600–5000 | 404.9 ± 9.1 | 383.1–451.5 |
| | Flight 04 | 10 September 2018 | 05:09–07:49 | 38.0–38.5 | 114.4–114.7 | 0–4600 | 405.0 ± 9.3 | 381.7–455.5 |
| | Flight 05 | 10 September 2018 | 11:17–13:12 | 38.0–38.3 | 114.4–114.7 | 600–2800 | 400.9 ± 9.6 | 376.3–441.9 |
| | Flight 06 | 12 September 2018 | 12:12–12:44 | 38.0–38.3 | 114.4–114.8 | 0–2800 | 428.8 ± 37.2 | 376.0–543.7 |
| | Flight 07 | 14 September 2018 | 03:13–06:10 | 38.0–38.4 | 114.4–114.8 | 0–5200 | 414.6 ± 18.0 | 394.8–523.1 |
| | Flight 08 | 14 September 2018 | 10:53–14:13 | 38.0–38.4 | 114.4–114.8 | 0–5000 | 413.4 ± 17.4 | 380.8–509.1 |
| | Flight 09 | 7 January 2019 | 11:00–18:06 | 38.0–38.4 | 114.4–114.7 | 0–5400 | 409.4 ± 12.9 | 377.7–457.2 |
| Winter | Flight 10 | 8 January 2019 | 03:25–04:58 | 38.0–38.4 | 114.4–114.7 | 0–5100 | 410.6 ± 9.9 | 390.4–457.0 |
| | Flight 11 | 11 January 2019 | 02:47–06:24 | 38.0–38.4 | 114.4–114.9 | 0–5300 | 443.8 ± 31.8 | 403.9–555.0 |
| | Flight 12 | 12 January 2019 | 05:48–09:21 | 38.0–38.5 | 114.4–114.7 | 1100–5000 | 409.8 ± 6.1 | 380.5–438.5 |

2.3. Data Processing

2.3.1. Screening of Invalid Data

During the flight, data anomalies caused by atmospheric turbulence and special weather conditions were marked and removed. These data were not involved in the analysis.

2.3.2. Correction of the Detention Time

During the observations, the air samples entered an air intake hole at the top of the sampling head of the aircraft and entered the CRDS instrument through a certain length of air intake pipe to generate data. The sample time recorded with the equipment lagged behind the real sampling time. According to the calculation of the pipeline's volume and the sampling flow, the detention time was 10 s, and the normal cruising speed of the aircraft was about 60 m/s. If the error was not corrected, the error reached as high as 600 m. Therefore, the detention time needed to be corrected when the geographic information from the GPS corresponded to the observed concentrations.

2.3.3. Calibration of the CRDS Instrument

In order to ensure the accuracy of the collected data, the airborne CRDS greenhouse gas analyzer was calibrated with a standard gas that was traceable to the Central Calibration Laboratory (CCL) of the World Meteorological Organization (WMO) before the flight, and the observation data were corrected according to the results of the calibration with standard gases. The observational CO₂ could be traced to the standard scales of WMO X2007 and WMO X2014A.

2.3.4. Data Processing

According to changes in the altitude detected by the aircraft, the concentrations of CO₂ in the vertical direction were averaged every 10 m to obtain the vertical profile for both the ascending and descending stages of the flights.

2.4. TrajStat Model for the Calculation of the Backward Trajectory

TrajStat (Trajectory Statistics) is a kind of Lagrange particle diffusion model that was originally developed based on the NOAA Hybrid Single-Particle Lagrangian Integrated Trajectory (HYSPPLIT) model (<http://ready.arl.noaa.gov/HYSPLIT.php>, accessed on 28 September 2023) [35]. TrajStat has a geographic information system (GIS), the user-friendly GUI of which makes it much more visually convenient and intuitive for users to calculate backward/forward trajectories and estimate the potential sources of air pollutants based on a potential source contribution function (PSCF) or concentration weighted trajectory (CWT). In this study, an archival dataset of 1° × 1° Global Data Assimilation System (GDAS) data from 2018–2019 was downloaded from the website of the National Centers for Environmental Prediction (NCEP) (<https://www.ready.noaa.gov/archives.php>, accessed

on 28 September 2023) and used to calculate a 72 h backward trajectory [36]. In order to explore the impacts of different heights on transport, we set the arrival points at 500 m, 1000 m, 2000 m, 3000 m, and 4000 m above Shijiazhuang city, respectively.

3. Results

3.1. The Tropospheric Distribution of CO₂ on the North China Plain

The spatio-temporal distributions of CO₂ (ppm) during the measurements of the 12 flights are shown in Figure 3. The individual vertical averages of CO₂ concentrations for the 12 flights were 399.9 ± 1.5 ppm, 404.4 ± 6.7 ppm, 404.9 ± 9.1 ppm, 405.0 ± 9.3 ppm, 400.9 ± 9.6 ppm, 428.8 ± 37.2 ppm, 414.6 ± 18.0 ppm, 413.4 ± 17.4 ppm, 409.4 ± 12.9 ppm, 410.6 ± 9.9 ppm, 443.8 ± 31.8 ppm, and 409.8 ± 6.1 ppm, respectively. We compared the measurements with in situ measurements of the global-scale average and those from atmospheric background stations, such as Mauna Loa at low latitude (Hawaii, HI, USA), Waliguan at middle latitude (Qinghai, China), and Shangdianzi (North China Plain). The global average concentration of CO₂ was estimated to be 410.5 ± 0.20 ppm in 2019, which was slightly lower than the two background concentrations of 411.6 ± 2.1 ppm and 411.4 ± 0.2 ppm in Mauna Loa and Waliguan. The similar levels in the two stations reflect the background concentration in the free atmosphere with a large scale of uniform mixing. However, at Shangdianzi station, which is regarded as representative of the near-surface CO₂ concentration in the North China Plain, the concentration of 420.2 ± 0.3 ppm was 2.36% higher than the global level and 2.11% higher than the background levels at Mauna Loa and Waliguan, indicating the severe level of anthropogenic emissions in this mega-agglomeration. In addition, the level in Shangdianzi was also found to lie between the aircraft-observed vertical averages of 399.9 and 443.8 ppm. In addition to these in situ measurements, satellite remote sensing was also capable of obtaining the columnar mean concentrations, and they were 408.0 ± 2.2 ppm and 409.8 ± 2.0 ppm for both the world and China in 2019. The levels were similar with those of 409.4 ± 12.9 ppm, 410.6 ± 9.9 ppm, and 409.8 ± 6.1 ppm measured on 7, 8, and 12 January 2019.

3.2. The Impact of Tropospheric Thermal Stratification on the Vertical CO₂

On the basis of concurrent thermodynamic measurements of temperature and pressure, the potential temperature θ was retrieved and plotted along with the CO₂ concentration (Figure 4). The three layers of these θ profiles, i.e., the inversion layer (IL, blue), planetary boundary layer (PBL, black), and nighttime residual layer (RL, black), are highlighted in the panels of Figure 4. In consideration of the absence of observations of the low troposphere on Flights 01 (8 September 2018), 03 (9 September 2018), 05 (10 September 2018), and 12 (12 January 2019), the PBL heights (PBLHs) were only estimated for the other eight flights, and there was no shortage of observations. To ensure comparability, the profile data were averaged into 100 m altitude bins, and the value in every given bin was the mean of all points in that range.

The PBLHs were approximately 800 m, 300 m (night, and 1100 m for the RL height), 1200 m, 300 m (night, and 900 m for the RL height), 700 m, 600 m, 600 m, and 600 m on Flights 02, 04, 06, 07, 08, 09, 10, and 11. The average CO₂ concentrations below the PBLH were 403.4 ppm, 423.8 ppm (429.6 ppm below the RLH), 453.2 ppm, 443.8 ppm (436.7 ppm), and 450.5 ppm for autumn, and they were 414.9 ppm, 440.6 ppm, and 477.4 ppm for winter. Above the PBLH, these values were 406.6 ppm, 411.3 ppm (406.4 ppm), 433.5 ppm, 408.8 ppm (434.5 ppm), and 405.8 ppm in autumn and 407.8 ppm, 409.8 ppm, and 449.7 ppm in winter. According to the statistics, it was found that the mean CO₂ concentrations below the PBLH were -0.79% , 3.04% (5.73%), 4.54% , 8.56% (0.51%), and 11.02% higher than those above the PBLH in autumn and 1.74% , 7.52% , and 6.16% higher than those above the PBLH in winter. Therefore, except for the case of Flight 01 (i.e., 8 September 2018), the CO₂ concentration was significantly higher within the PBL, showing that the PBLH and RLH were particularly important in constraining the CO₂ and may contribute to the more powerful atmospheric heating effects.

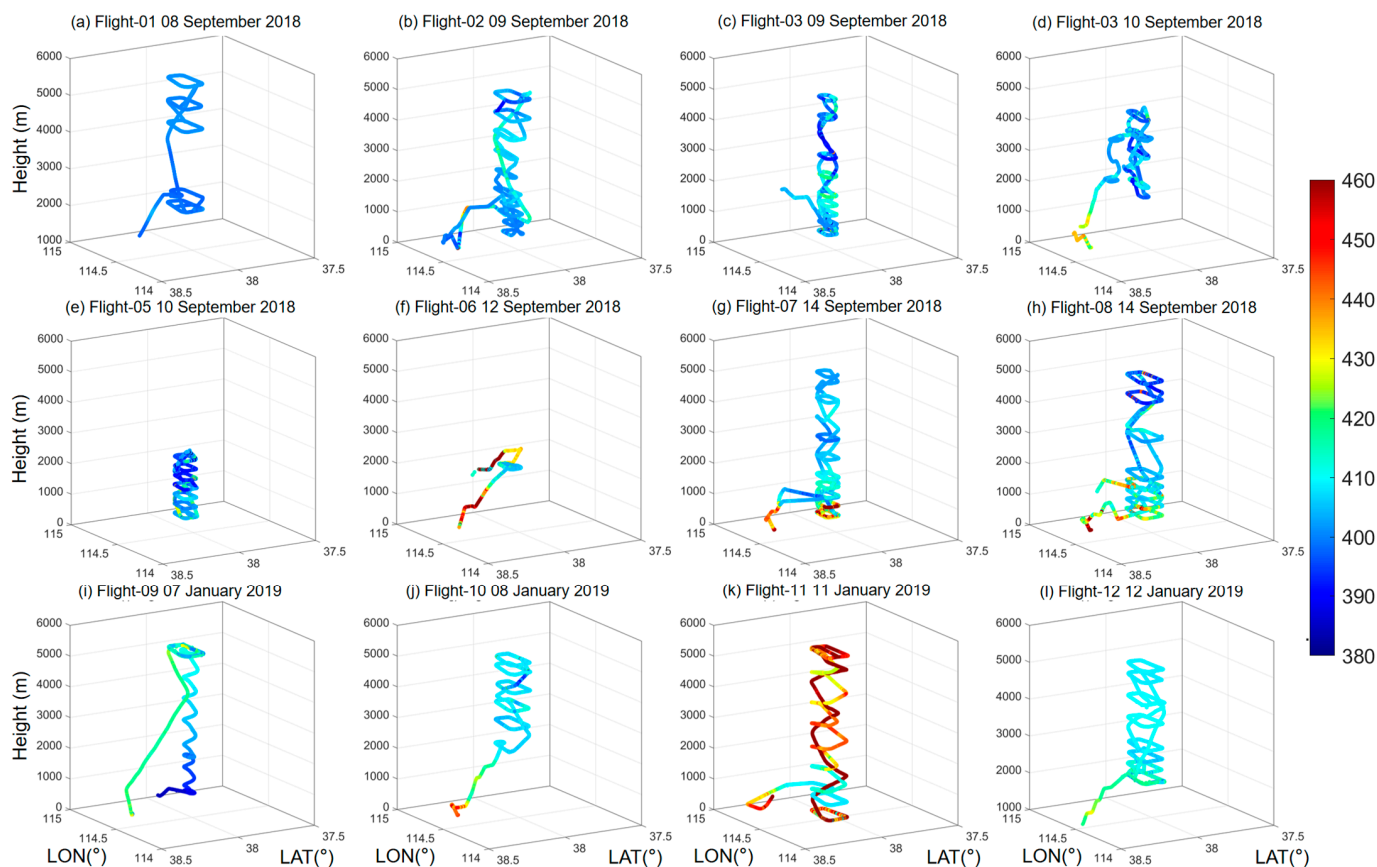


Figure 3. Three-dimensional distribution of CO₂ (ppm) measured during (a) Flight 01 (8 September 2018), (b) Flight 02 (9 September 2018), (c) Flight 03 (9 September 2018), (d) Flight 04 (10 September 2018), (e) Flight 05 (10 September 2018), (f) Flight 06 (12 September 2018), (g) Flight 07 (14 September 2018), (h) Flight 08 (14 September 2018), (i) Flight 09 (7 January 2019), (j) Flight 10 (8 January 2019), (k) Flight 11 (11 January 2019), and (l) Flight 12 (12 January 2019).

Another important stratification in the atmosphere is the IL—especially the elevated IL—as it induces similar constraining effects to those of the PBL [37], as shown in Figure 4a,c,e,l. The elevated IL is generally accompanied by strong stability, so it is also feasible for high levels of CO₂ concentrations to be captured. Therefore, it can be concluded that both the PBLH (RLH) and ILH are likely to be very crucial in determining the vertical distributions of CO₂, leading to some potential influences on the thermal structures of the troposphere. This is also particularly important in the field of the PBL physico-chemical process [38–40].

3.3. The Backward Trajectories and Potential Influences of Transport

With the aim of investigating the potential influences of transport processes, we retrieved the backward trajectories at the arrival heights of 500 m, 1000 m, 2000 m, 3000 m, 4000 m, and 5000 m for each flight day using the advanced TrajStat model, as shown in Figures 5 and 6. With the assistance of these backward air masses, the potential contributions of long-distance transport to the vertical distributions of CO₂ were quantitatively assessed in each season.

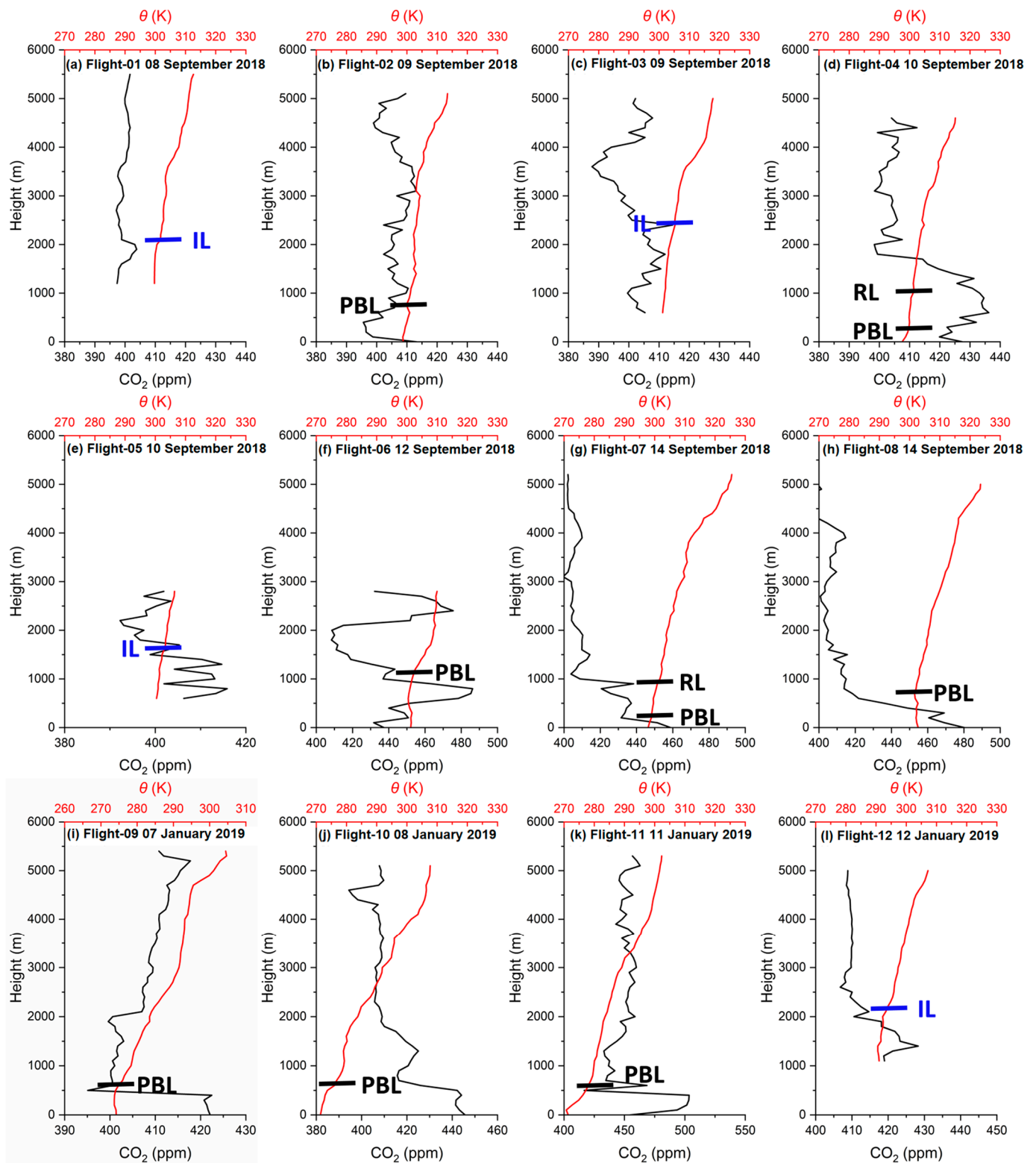


Figure 4. Vertically averaged levels of CO₂ (ppm) and the potential temperature θ (K) in bins of 100 m for 12 flights: (a) Flight 01 (8 September 2018), (b) Flight 02 (9 September 2018), (c) Flight 03 (9 September 2018), (d) Flight 04 (10 September 2018), (e) Flight 05 (10 September 2018), (f) Flight 06 (12 September 2018), (g) Flight 07 (14 September 2018), (h) Flight 08 (14 September 2018), (i) Flight 09 (7 January 2019), (j) Flight 10 (08 January 2019), (k) Flight 11 (11 January 2019), and (l) Flight 12 (12 January 2019). Abbreviations: IL (inversion layer), RL (residual layer), and PBL (planetary boundary layer).

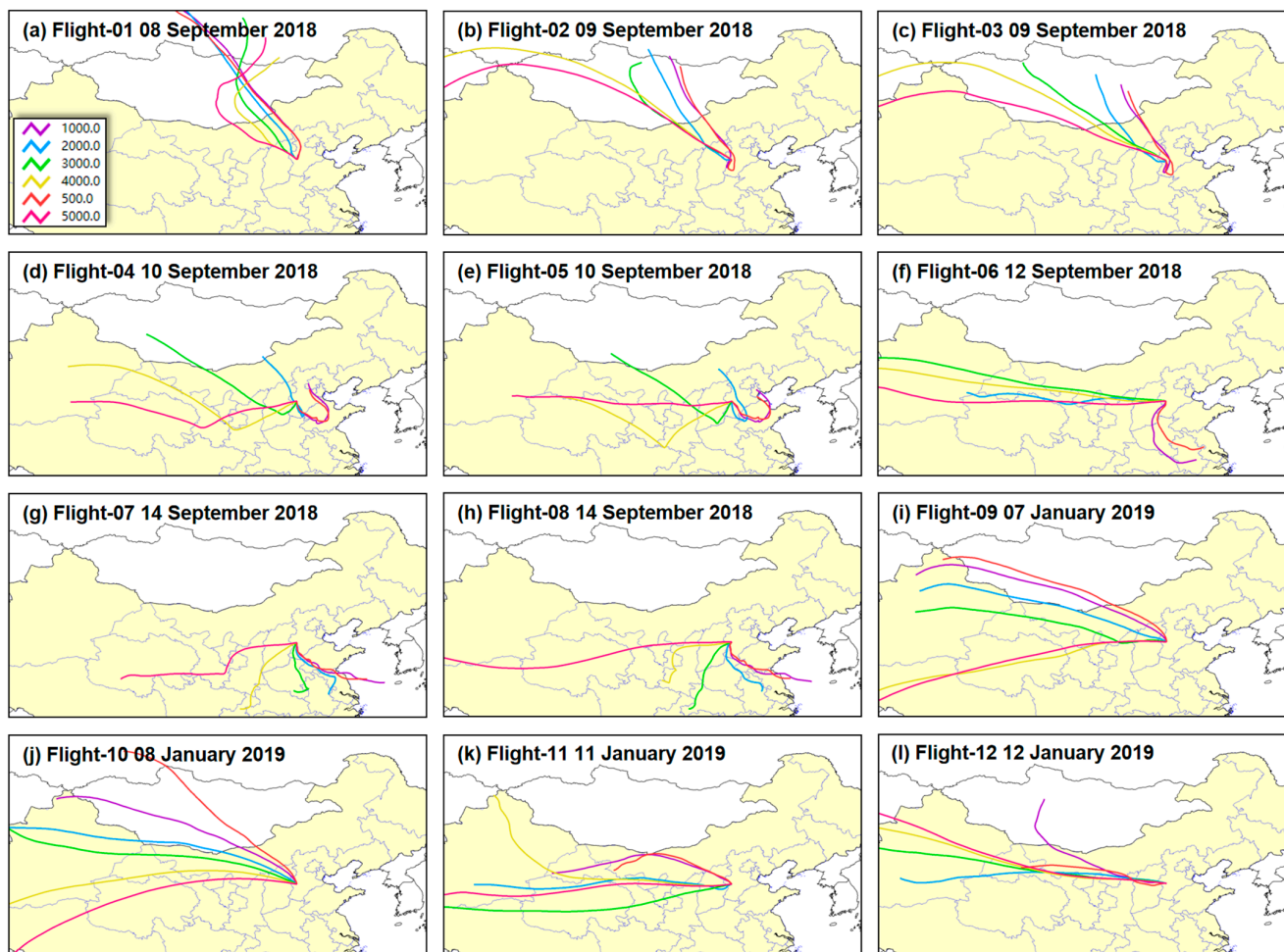


Figure 5. The backward trajectories in Shijiazhuang City on the 12 flight days. The different colors denote the arrival points of 500 m (red), 1000 m (purple), 2000 m (blue), 3000 m (green), 4000 m (yellow), and 5000 m (pink) in different flights of (a) Flight 01 (8 September 2018), (b) Flight 02 (9 September 2018), (c) Flight 03 (9 September 2018), (d) Flight 04 (10 September 2018), (e) Flight 05 (10 September 2018), (f) Flight 06 (12 September 2018), (g) Flight 07 (14 September 2018), (h) Flight 08 (14 September 2018), (i) Flight 09 (7 January 2019), (j) Flight 10 (08 January 2019), (k) Flight 11 (11 January 2019), and (l) Flight 12 (12 January 2019).

- Autumn (Figure 5a–h): The air masses were grouped into three different categories, i.e., group 1 containing Flights 01 (8 September 2018), 02 (9 September 2018), and 03 (9 September 2018); group 2 containing Flights 04 (10 September 2018) and 05 (10 September 2018); and group 3 containing Flights 06 (12 September 2018), 07 (14 September 2018), and 08 (14 September 2018). In the first category, the air masses all came from outer Mongolia and Russia, under the influence of which the vertical distributions of CO₂ behaved with relatively small fluctuations or vertical homogeneity. Only the air masses arriving at 500 m and 1000 m were associated with the PBL during the transporting processes, i.e., the heights of these trajectories can be lower than 1000 m (Flights 01–03 in Figure 6a–c), but they have minimal influences on the vertical CO₂ because of the lack of anthropogenic sources. In the second category, the air trajectories at 2000 m, 3000 m, 4000 m, and 5000 m were still from the western and northwestern regions, whereas the low-altitude trajectories at 500 m and 1000 m were almost all from local transport within the area of the North China Plain, lower than 1000 m for most of the time along the transport paths (Flights 04–05 in Figure 6d,e). In the last group, these air masses started to change directions, with air masses in the PBL coming from southern areas of the North China Plain—Shandong Province, Henan Province, and Jiangsu Province—and

the air masses originated from the western and southern areas. Except for the two PBL trajectories transported below 1000 m (Flights 06–08 in Figure 6f–h), the air mass arriving at 2000 m also originated from the low altitude of about 440 m, which was very likely to contribute to the CO₂ peak at around 2400 m (Flight 06 in Figure 4f). This evidenced that the vertical mixing during transport can account for some layers of high CO₂ concentration aloft. Considering the latter two groups, as well as the vertical CO₂ levels, we reached the conclusion that the PBL trajectories from the local area and the densely populated areas to the south all will increase the concentration of CO₂ because of intensive anthropogenic emissions, but in general, the mid-tropospheric CO₂ was homogeneously distributed, reflecting the seasonal atmospheric background state.

- Winter (Figure 5i–l): The air trajectories for the five different heights on the four flight days all came from western origins. Similarly, the PBL trajectories from the western and northwestern areas contributed to the high CO₂ levels below the height of 1000 m, although they only went as low as 1000 m within the backward 24 h (Flights 09–12 in Figure 6i–l). This phenomenon was closely associated with coal-burning emissions for winter heating in northern China. In the middle troposphere, the air masses had minimal influences on the CO₂ levels, except for the case of Flight 09, in which the path that lifts air from below 1 km at the start up to 4 km at the receptor might partly explain the aloft inverted profile (Figure 4i).

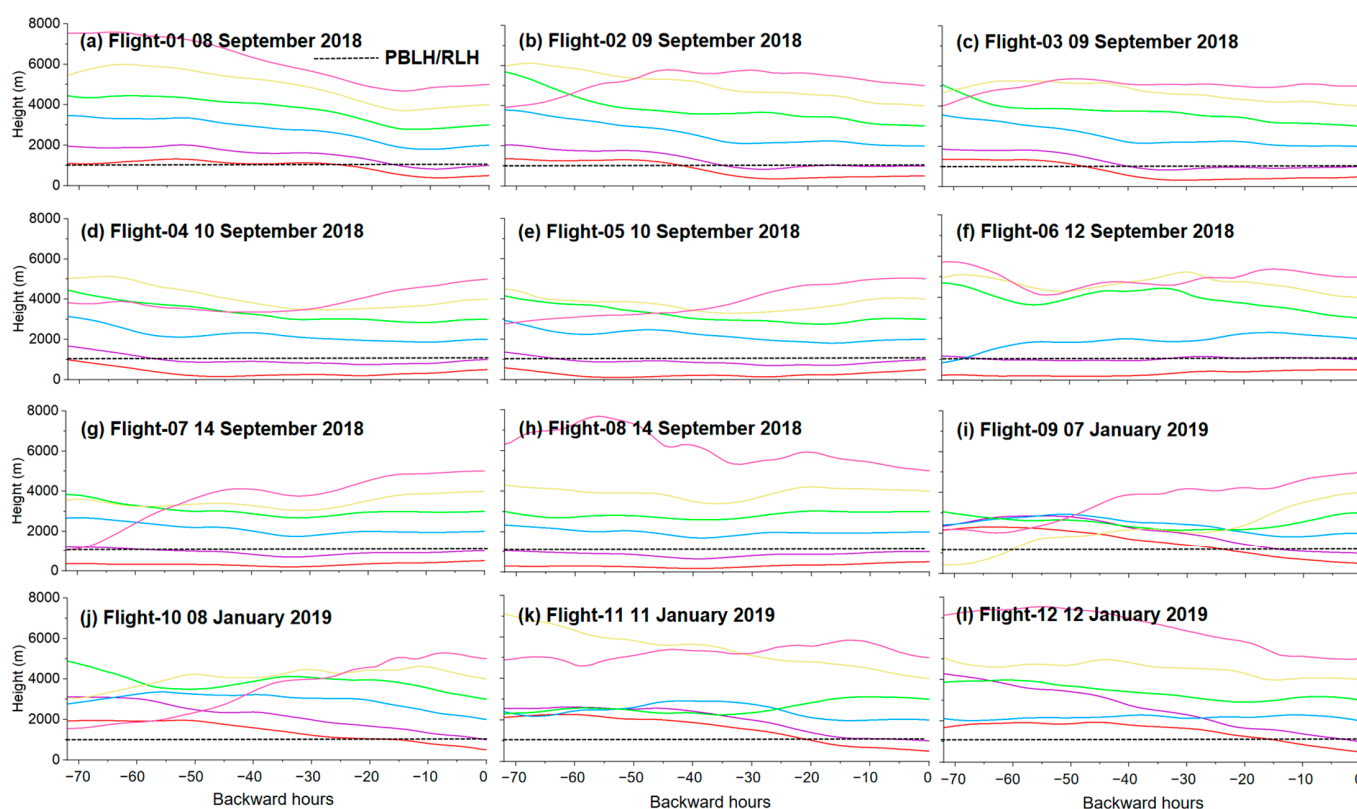


Figure 6. The heights of the 72 h backward trajectories in Shijiazhuang City on the 12 flight days of (a) Flight 01 (8 September 2018), (b) Flight 02 (9 September 2018), (c) Flight 03 (9 September 2018), (d) Flight 04 (10 September 2018), (e) Flight 05 (10 September 2018), (f) Flight 06 (12 September 2018), (g) Flight 07 (14 September 2018), (h) Flight 08 (14 September 2018), (i) Flight 09 (7 January 2019), (j) Flight 10 (8 January 2019), (k) Flight 11 (11 January 2019), and (l) Flight 12 (12 January 2019). The different colors denote the arrival points of 500 m (red), 1000 m (purple), 2000 m (blue), 3000 m (green), 4000 m (yellow), and 5000 m (pink). The dashed lines represent the ideal PBLH or RLH of 1000 m. PBLH: planetary boundary layer height; RLH: residual layer height.

In summary, there were consistently higher CO₂ concentrations within the PBL regardless of the season, and there were homogeneous CO₂ distributions throughout the middle troposphere. As shown in Table 2 and Figure 7, in autumn, the mean values for the altitudes of 0–500 m and 500–1000 m were 441.0 ppm and 425.0 ppm, with a minimal fluctuation of 401.7–408.3 ppm in the middle troposphere. In winter, the CO₂ concentrations were 441.7 ppm (0–500 m) and 416.8 ppm (500–1000 m), whereas the level in the middle troposphere varied from 412.0 ppm to 419.2 ppm. As a consequence, we reached the conclusion that similar levels below the PBL were observed for the two seasons, but the mid-tropospheric CO₂ concentration was significantly higher in winter than in autumn, which can be explained by the concentration in the free troposphere following the global seasonal pattern, with a summer minimum and winter maximum. It was driven by the seasonality of the net CO₂ exchange and the balance between photosynthesis and respiration, but on a global scale, there was a latitudinal dependence.

Table 2. The average values of CO₂ at different altitudes of 0–500 m, 500–1000 m, 1000–2000 m, 2000–3000 m, 3000–4000 m, and 4000–5000 m.

| CO ₂ | DATE | 0–500 m | 500–1000 m | 1000–2000 m | 2000–3000 m | 3000–4000 m | 4000–5000 m | |
|-----------------|-----------|-------------------|------------|-------------|-------------|-------------|-------------|-------|
| Autumn | Flight 01 | 8 September 2018 | - | - | 399.6 | 398.5 | 399.3 | 400.7 |
| | Flight 02 | 9 September 2018 | 418.3 | 402.8 | 404.7 | 404.5 | 407.8 | 401.7 |
| | Flight 03 | 9 September 2018 | - | 403.7 | 408.9 | 410.1 | 396.3 | 401.5 |
| | Flight 04 | 10 September 2018 | 426.2 | 433.9 | 411.0 | 405.1 | 402.2 | 401.2 |
| | Flight 05 | 10 September 2018 | - | 405.1 | 401.3 | 396.0 | - | - |
| | Flight 06 | 12 September 2018 | 442.1 | 474.6 | 420.7 | 423.4 | - | - |
| | Flight 07 | 14 September 2018 | 444.0 | 435.1 | 408.4 | 405.2 | 402.2 | 404.9 |
| | Flight 08 | 14 September 2018 | 474.1 | 419.7 | 412.1 | 403.2 | 407.3 | 400.1 |
| | Average | | 441.0 | 425.0 | 408.3 | 405.8 | 402.5 | 401.7 |
| Winter | Flight 09 | 7 January 2019 | 422.1 | 390.5 | 400.9 | 405.3 | 409.8 | 412.8 |
| | Flight 10 | 8 January 2019 | 443.5 | 437.8 | 418.2 | 407.2 | 407.9 | 406.9 |
| | Flight 11 | 11 January 2019 | 459.6 | 422.0 | 441.9 | 454.6 | 453.7 | 449.1 |
| | Flight 12 | 12 January 2019 | - | - | 423.1 | 409.8 | 410.1 | 409.1 |
| | Average | | 441.7 | 416.8 | 421.0 | 419.2 | 420.4 | 419.5 |

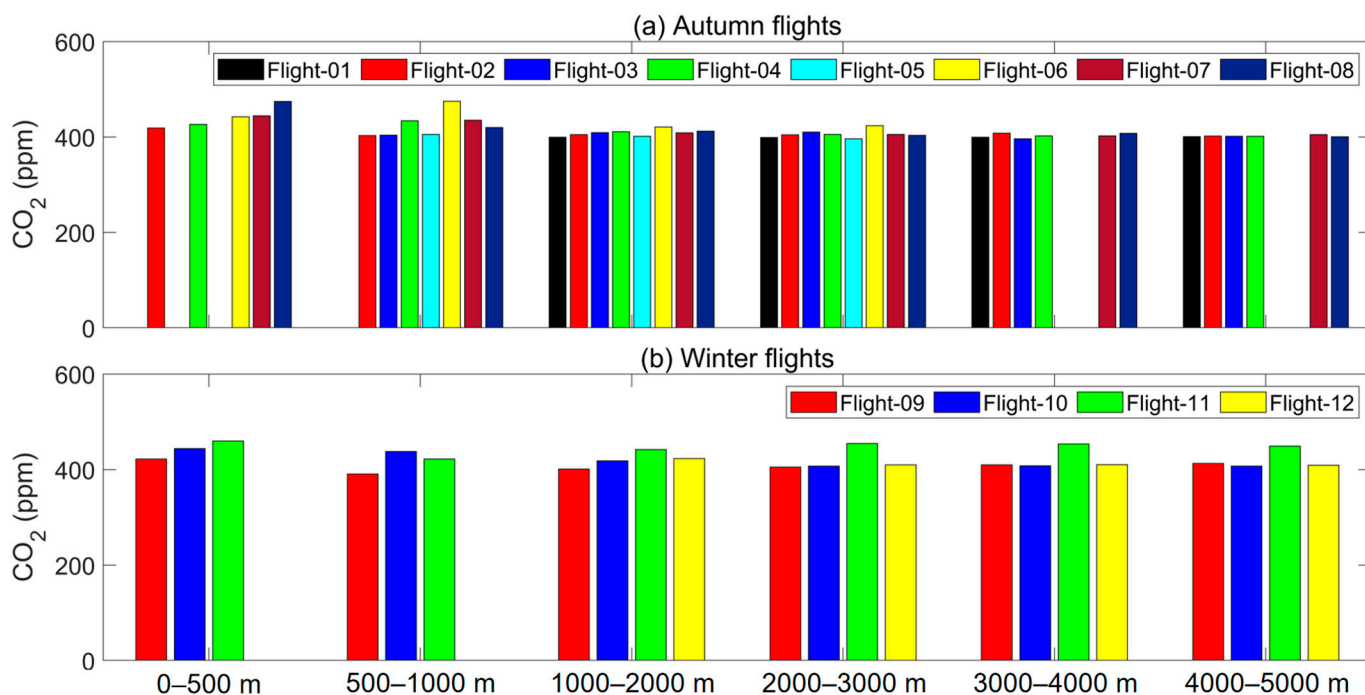


Figure 7. The average values of CO₂ at the different altitudes of 0–500 m, 500–1000 m, 1000–2000 m, 2000–3000 m, 3000–4000 m, and 4000–5000 m in (a) autumn and (b) winter.

4. Conclusions and Outlooks

4.1. Main Conclusions

In this study, vertical concentration profiles of the tropospheric CO₂ over Shijiazhuang city in the North China Plain were measured on 12 aircraft flights during the autumn and winter of 2018 and 2019. The tropospheric distributions of CO₂ and their relations with the atmospheric thermodynamic stratification were systemically reported for the first time. The conclusions are summarized as follows.

- (1) The vertical averages measured with the aircraft were in a broad range from 399.9 to 443.8 ppm. This level was slightly higher than the background levels at low-latitude Mauna Loa and mid-latitude Waliguan, as well as the global columnar concentration measured with a satellite, indicating the severe anthropogenic emissions in this mega-agglomeration.
- (2) Both the IL and PBL (or RL) were crucial in constraining the high CO₂ concentrations. This implies that the long-wave heating effect of CO₂ within the PBL may also play a non-negligible role in regulating the thermal structure of the low troposphere; in particular, during the nighttime, the atmospheric warming effect might reduce the occurrence of the surface stable boundary layer, which enhances the atmospheric diffusion.
- (3) There were three different categories of air masses in autumn and one category in winter. The low-altitude PBL trajectories from both local areas and densely populated areas to the south in autumn increased the CO₂ due to severe anthropogenic emissions, but in winter, the air masses in the PBL from western areas all contribute to an increase of CO₂. Throughout the middle troposphere, the CO₂ concentrations were usually homogeneously distributed regardless of their origins, but this heavily depended on the season. The high CO₂ concentrations in winter can be explained by the concentration in the free troposphere following the global seasonal pattern of summertime lower values and wintertime high values. This was driven by the seasonality of the net CO₂ exchange and the balance between photosynthesis and respiration, but on a global scale, there is a latitudinal dependence.

4.2. Outlooks and Discussion

In this study, only flights in regions of urban agglomerations on the North China Plain were conducted, but no measurements were conducted in carbon source areas, such as forests, grasslands, and mountains. This limits our understanding of the spatial distribution of CO₂ in carbon source regions, as well as other ecosystems.

Referring to the Global Greenhouse Gas Reference Network's aircraft program, which is managed by the NOAA, we recommend building a national-scale aircraft network across China to perform long-term, organized, and unified flight observations of not only GHGs, but also other chemical species in different ecosystems. These potentially valuable data are particularly important in constraining models of both weather and the environment.

In summary, the conclusions reached in this study offer scientific references and valuable datasets for the evaluation of carbon accounting and carbon emissions, as well as for driving and validating climate models. Furthermore, for future perspectives, we highlight the potential importance of increasing CO₂ concentrations in regulating the PBL's structures, particularly in the field of research on the atmospheric environment, such as in studies of aerosol–PBL interactions.

Author Contributions: Conceptualization, H.Z., Q.Y. and X.H.; methodology, H.Z., Q.Y., H.Y., D.M., Z.L., J.J. and B.L.; software, H.Z., G.W., L.D. and X.H.; validation, N.Z., H.S. and Y.S.; formal analysis, H.Z., Q.Y., H.Y., Y.M., L.D. and X.H.; investigation, H.Z., Y.M., L.D. and X.H.; resources, H.Y., D.M., Z.L., J.J., G.W., N.Z., H.S., Y.S. and B.L.; data curation, Q.Y., H.Y., D.M., Z.L. and B.L.; writing—original draft preparation, H.Z., Q.Y. and X.H.; writing—review and editing, H.Z., Y.M., L.D. and X.H.; visualization, H.Z., Q.Y., Y.M. and L.D.; supervision, Y.M., L.D. and X.H.; project administration, H.Z., Q.Y. and B.L.; funding acquisition, H.Z. and L.D. All authors have read and agreed to the published version of the manuscript.

Funding: This study was supported by the Key Research and Development Program of Tangshan City (22150223J), the Science and Technology Project of Beijing Meteorological Service (BMBKJ202201004), and the Basic R&D Special Fund for the Central Level of Scientific Research Institutes (TUMKY202213).

Institutional Review Board Statement: Not applicable.

Informed Consent Statement: Not applicable.

Data Availability Statement: The data presented in this study are available on request from the corresponding author.

Conflicts of Interest: The authors declared that they have no conflicts of interests. The Beijing Jiangbo Environmental Technology Co., Ltd., had no role in the design of the study; in the collection, analyses, or interpretation of data; in writing of the manuscript, or in the decision to publish results.

References

1. Le Quéré, C.; Jackson, R.B.; Jones, M.W.; Smith, A.J.P.; Abernethy, S.; Andrew, R.M.; De-Gol, A.J.; Willis, D.R.; Shan, Y.; Canadell, J.G.; et al. Temporary reduction in daily global CO₂ emissions during the COVID-19 forced confinement. *Nat. Clim. Chang.* **2020**, *10*, 647–653. [CrossRef]
2. Ballantyne, A.P.; Alden, C.B.; Miller, J.B.; Tans, P.P.; White, J.W.C. Increase in observed net carbon dioxide uptake by land and oceans during the last 50 years. *Nature* **2012**, *488*, 70–72. [CrossRef]
3. Andres, R.J.; Boden, T.A.; Bréon, F.-M.; Ciais, P.; Davis, S.; Erickson, D.; Gregg, J.S.; Jacobson, A.; Marland, G.; Miller, J.; et al. A synthesis of carbon dioxide emissions from fossil-fuel combustion. *Biogeosciences* **2012**, *9*, 1845–1871. [CrossRef]
4. Peters, G.P.; Andrew, R.M.; Canadell, J.G.; Friedlingstein, P.; Jackson, R.B.; Korsbakken, J.I.; Le Quéré, C.; Pregon, A. Carbon dioxide emissions continue to grow amidst slowly emerging climate policies. *Nat. Clim. Chang.* **2020**, *10*, 3–6. [CrossRef]
5. Nyambuu, U.; Semmler, W. Climate change and the transition to a low carbon economy—Carbon targets and the carbon budget. *Econ. Model.* **2019**, *84*, 367–376. [CrossRef]
6. IPCC. Climate Change 2013: The Physical Science Basis. In *Contribution of Working Group I to the Fifth Assessment Report of the Intergovernmental Panel on Climate Change*; Stocker, T.F., Qin, D., Plattner, G.-K., Tignor, M., Allen, S.K., Boschung, J., Nauels, A., Xia, Y., Bex, V., Midgley, P.M., Eds.; Cambridge University Press: Cambridge, UK; New York, NY, USA, 2013; p. 1535.
7. Available online: www.esrl.noaa.gov/gmd/ccgg/trends/ (accessed on 28 September 2023).
8. Jones, M.W.; Andrew, R.M.; Peters, G.P.; Janssens-Maenhout, G.; De-Gol, A.J.; Ciais, P.; Patra, P.K.; Chevallier, F.; Le Quéré, C. Gridded fossil CO₂ emissions and related O₂ combustion consistent with national inventories 1959–2018. *Sci. Data* **2021**, *8*, 2. [CrossRef]
9. Edenhofer, O.; Kadner, S.; von Stechow, C.; Schwerhoff, G.; Luderer, G. Linking climate change mitigation research to sustainable development. In *Handbook of Sustainable Development*, 2nd ed.; Atkinson, G., Dietz, S., Neumayer, E., Agarwala, M., Eds.; Edward Elgar Publishing Limited: Cheltenham, UK, 2014.
10. Houghton, R.A.; House, J.I.; Pongratz, J.; Van Der Werf, G.R.; DeFries, R.S.; Hansen, M.C.; Le Quéré, C.; Ramankutty, N. Carbon emissions from land use and land-cover change. *Biogeosciences* **2012**, *9*, 5125–5142. [CrossRef]
11. Van Minnen, J.G.; Goldewijk, K.K.; Stehfest, E.; Eickhout, B.; van Drecht, G.; Leemans, R. The importance of three centuries of land-use change for the global and regional terrestrial carbon cycle. *Clim. Chang.* **2009**, *97*, 123–144. [CrossRef]
12. Kunik, L.; Mallia, D.V.; Gurney, K.R.; Mendoza, D.L.; Oda, T.; Lin, J.C. Bayesian inverse estimation of urban CO₂ emissions: Results from a synthetic data simulation over Salt Lake City, UT. *Elem. Sci. Anthr.* **2019**, *7*, 36. [CrossRef]
13. Pitt, J.R.; Lopez-Coto, I.; Hajny, K.D.; Tomlin, J.; Kaeser, R.; Jayarathne, T.; Stirm, B.H.; Floerchinger, C.R.; Loughner, C.P.; Gately, C.K.; et al. New York City greenhouse gas emissions estimated with inverse modeling of aircraft measurements. *Elem. Sci. Anthr.* **2022**, *10*, 1. [CrossRef]
14. Metya, A.; Datye, A.; Chakraborty, S.; Tiwari, Y.K.; Sarma, D.; Bora, A.; Gogoi, N. Diurnal and seasonal variability of CO₂ and CH₄ concentration in a semi-urban environment of western India. *Sci. Rep.* **2021**, *11*, 2931. [CrossRef] [PubMed]
15. Zeng, J.; Matsunaga, T.; Tan, Z.-H.; Saigusa, N.; Shirai, T.; Tang, Y.; Peng, S.; Fukuda, Y. Global terrestrial carbon fluxes of 1999–2019 estimated by upscaling eddy covariance data with a random forest. *Sci. Data* **2020**, *7*, 313. [CrossRef] [PubMed]
16. Jung, M.; Schwalm, C.; Migliavacca, M.; Walther, S.; Camps-Valls, G.; Koirala, S.; Anthoni, P.; Besnard, S.; Bodesheim, P.; Carvalhais, N.; et al. Scaling carbon fluxes from eddy covariance sites to globe: Synthesis and evaluation of the FLUXCOM approach. *Biogeosciences* **2020**, *17*, 1343–1365. [CrossRef]
17. Tramontana, G.; Jung, M.; Schwalm, C.R.; Ichii, K.; Camps-Valls, G.; Ráduly, B.; Reichstein, M.; Arain, M.A.; Cescatti, A.; Kiely, G.; et al. Predicting carbon dioxide and energy fluxes across global FLUXNET sites with regression algorithms. *Biogeosciences* **2016**, *13*, 4291–4313. [CrossRef]
18. Crosson, E.R. A cavity ring-down analyzer for measuring atmospheric levels of methane, carbon dioxide, and water vapor. *Appl. Phys. B* **2008**, *92*, 403–408. [CrossRef]
19. Song, S.; Wu, Y.; Xu, J.; Ohara, T.; Hasegawa, S.; Li, J.; Yang, L.; Hao, J. Black carbon at a roadside site in Beijing: Temporal variations and relationships with carbon monoxide and particle number size distribution. *Atmos. Environ.* **2013**, *77*, 213–221. [CrossRef]

20. Li, Y.; Ma, Z.; Han, T.; Quan, W.; Wang, J.; Zhou, H.; He, D.; Dong, F. Long-term declining in carbon monoxide (CO) at a rural site of Beijing during 2006–2018 implies the improved combustion efficiency and effective emission control. *J. Environ. Sci.* **2020**, *115*, 432–442. [[CrossRef](#)] [[PubMed](#)]
21. Xiao, J.; Chevallier, F.; Gomez, C.; Guanter, L.; Hicke, J.A.; Huete, A.R.; Ichii, K.; Ni, W.; Pang, Y.; Rahman, A.F.; et al. Remote sensing of the terrestrial carbon cycle: A review of advances over 50 years. *Remote Sens. Environ.* **2019**, *233*, 111383. [[CrossRef](#)]
22. Sasai, T.; Ichii, K.; Yamaguchi, Y.; Nemani, R. Simulating terrestrial carbon fluxes using the new biosphere model “bio-sphere model integrating eco-physiological and mechanistic approaches using satellite data” (BEAMS). *J. Geophys. Res. Biogeosciences* **2005**, *110*, G02014. [[CrossRef](#)]
23. Ma, Y.; Ye, J.; Ribeiro, I.O.; Vilà-Guerau de Arellano, J.; Xin, J.; Zhang, W.; Souza, R.A.; Martin, S.T. Optimization and Representativeness of Atmospheric Chemical Sampling by Hovering Unmanned Aerial Vehicles Over Tropical Forests. *Earth Space Sci.* **2021**, *8*, e2020EA001335. [[CrossRef](#)]
24. Haszpra, L.; Barcza, Z.; Davis, K.J.; Tarczay, K. Long-term tall tower carbon dioxide flux monitoring over an area of mixed vegetation. *Agric. For. Meteorol.* **2005**, *132*, 58–77. [[CrossRef](#)]
25. Matthews, B.; Schume, H. Tall tower eddy covariance measurements of CO₂ fluxes in Vienna, Austria. *Atmos. Environ.* **2022**, *274*, 118941. [[CrossRef](#)]
26. Jarvi, L.; Rannik, Ü.; Kokkonen, T.V.; Kurppa, M.; Karppinen, A.; Kouznetsov, R.D.; Rantala, P.; Vesala, T.; Wood, C.R. Uncertainty of eddy covariance flux measurements over an urban area based on two towers. *Atmos. Meas. Tech.* **2018**, *11*, 5421–5438. [[CrossRef](#)]
27. Li, J.; Fu, Q.; Huo, J.; Wang, D.; Yang, W.; Bian, Q.; Duan, Y.; Zhang, Y.; Pan, J.; Lin, Y.; et al. Tethered balloon-based black carbon profiles within the lower troposphere of Shanghai in the 2013 East China smog. *Atmos. Environ.* **2015**, *123*, 327–338. [[CrossRef](#)]
28. Bao, Z.; Han, P.; Zeng, N.; Liu, D.; Cai, Q.; Wang, Y.; Tang, G.; Zheng, K.; Yao, B. Observation and modeling of vertical carbon dioxide distribution in a heavily polluted suburban environment. *Atmos. Ocean. Sci. Lett.* **2020**, *13*, 371–379. [[CrossRef](#)]
29. Guimarães, P.; Ye, J.; Batista, C.; Barbosa, R.; Ribeiro, I.; Medeiros, A.; Zhao, T.; Hwang, W.-C.; Hung, H.-M.; Souza, R.; et al. Vertical profiles of atmospheric species concentrations and nighttime boundary layer structure in the dry season over an urban environment in the central Amazon collected by an unmanned aerial vehicle. *Atmosphere* **2020**, *11*, 1371. [[CrossRef](#)]
30. Wu, J.; Yin, Y.; Chen, K.; He, C.; Jiang, H.; Zheng, B.; Li, B.; Li, Y.; Lv, Y. Vertical Distribution of Atmospheric Ice Nucleating Particles in Winter over Northwest China Based on Aircraft Observations. *Atmosphere* **2022**, *13*, 1447. [[CrossRef](#)]
31. Karion, A.; Sweeney, C.; Wolter, S.; Newberger, T.; Chen, H.; Andrews, A.; Kofler, J.; Neff, D.; Tans, P. Long-term greenhouse gas measurements from aircraft. *Atmos. Meas. Tech.* **2013**, *6*, 511–526. [[CrossRef](#)]
32. Available online: <https://gml.noaa.gov/ccgg/aircraft/> (accessed on 28 September 2023).
33. Gatti, L.V.; Miller, J.B.; D’Amelio, M.T.S.; Martinewski, A.; Basso, L.S.; Gloor, M.E.; Wofsy, S.; Tans, P. Vertical profiles of CO₂ above eastern Amazonia suggest a net carbon flux to the atmosphere and balanced biosphere between 2000 and 2009. *Tellus B* **2010**, *62*, 581–594. [[CrossRef](#)]
34. Cai, B.; Cui, C.; Zhang, D.; Cao, L.B.; Wu, P.C.; Pang, L.Y.; Zhang, J.H.; Dai, C.Y. *China Greenhouse Gases Emission 2015*; China Environmental Publishing Group: Beijing, China, 2019; pp. 74–75.
35. Wang, Y.Q.; Zhang, X.Y.; Draxler, R.R. TrajStat: GIS-based software that uses various trajectory statistical analysis methods to identify potential sources from long-term air pollution measurement data. *Environ. Model. Softw.* **2009**, *24*, 938–939. [[CrossRef](#)]
36. Xin, J.; Ma, Y.; Zhao, D.; Gong, C.; Ren, X.; Tang, G.; Xia, X.; Wang, Z.; Cao, J.; de Arellano, J.V.-G.; et al. The feedback effects of aerosols from different sources on the urban boundary layer in Beijing China. *Environ. Pollut.* **2023**, *235*, 121440. [[CrossRef](#)] [[PubMed](#)]
37. Ma, Y.; Ye, J.; Xin, J.; Zhang, W.; de Arellano, J.V.; Wang, S.; Zhao, D.; Dai, L.; Ma, Y.; Wu, X.; et al. The Stove, Dome, and Umbrella Effects of Atmospheric Aerosol on the Development of the Planetary Boundary Layer in Hazy Regions. *Geophys. Res. Lett.* **2020**, *47*, e2020GL087373. [[CrossRef](#)]
38. Wang, Y.; Yu, M.; Wang, Y.; Tang, G.; Song, T.; Zhou, P.; Liu, Z.; Hu, B.; Ji, D.; Wang, L.; et al. Rapid formation of intense haze episodes via aerosol-boundary layer feedback in Beijing. *Atmos. Chem. Phys.* **2020**, *20*, 45–53. [[CrossRef](#)]
39. Wang, Y.; Ma, Y.; Yan, C.; Yao, L.; Cai, R.; Li, S.; Lin, Z.; Zhao, X.; Yin, R.; Deng, C.; et al. Sulfur Dioxide Transported From the Residual Layer Drives Atmospheric Nucleation During Haze Periods in Beijing. *Geophys. Res. Lett.* **2023**, *50*, e2022GL100514. [[CrossRef](#)]
40. Zhao, T.; Ye, J.; Ribeiro, I.O.; Ma, Y.; Hung, H.-M.; Batista, C.E.; Stewart, M.P.; Guimarães, P.C.; de Arellano, J.V.-G.; de Souza, R.A.F.; et al. River winds and pollutant recirculation near the Manaus city in the central Amazon. *Commun. Earth Environ.* **2021**, *2*, 205. [[CrossRef](#)]

Disclaimer/Publisher’s Note: The statements, opinions and data contained in all publications are solely those of the individual author(s) and contributor(s) and not of MDPI and/or the editor(s). MDPI and/or the editor(s) disclaim responsibility for any injury to people or property resulting from any ideas, methods, instructions or products referred to in the content.